



Cite this: *Phys. Chem. Chem. Phys.*, 2016, 18, 1478

# Hybrid materials of ZnO nanostructures with reduced graphene oxide and gold nanoparticles: enhanced photodegradation rates in relation to their composition and morphology†

K. Bramhaiah,<sup>a</sup> Vidya N. Singh<sup>b</sup> and Neena S. John<sup>\*a</sup>

Binary and ternary hybrid systems of ZnO possessing nanoparticle and nanorod morphologies on reduced graphene oxide (rGO) and rGO with Au nanoparticles are explored as photocatalysts and a comparative study of their photodegradation performance is presented. Various preparation methods such as solution phase and hydrothermal routes have been employed to produce rGO–ZnO hybrids and rGO–Au–ZnO hybrids to impart different morphologies and defect states in ZnO. All the hybrids exhibit faster photodegradation kinetics and the rGO–Au–ZnO system exhibits the highest rate, five times faster than bare ZnO, followed by the binary systems, rGO–ZnO nanoparticles and nanorods. Various factors such as structure, morphology, charge transfer and adsorption are considered to explain the observed kinetics. Excited state electron transfer from ZnO to both rGO and Au levels facilitates faster dye degradation for rGO–Au–ZnO and is reflected as highly quenched band edge and defect state photoluminescence. Intimate physical interfaces formed between rGO, Au and ZnO in the hybrid material during *in situ* reactions favour charge transfer across the components. The charge transfer contribution even dominates the adsorption factor and the rGO–Au–ZnO system with a slightly lower adsorption capacity than the rGO–ZnO system exhibits a higher degradation rate. A power law dependence of the photodegradation rate on light intensity is also expressed.

Received 26th August 2015,  
Accepted 18th November 2015

DOI: 10.1039/c5cp05081b

www.rsc.org/pccp

## Introduction

Zinc oxide, a wide band gap semiconductor (3.37 eV) with strong absorption and luminescence in the ultraviolet (UV) region, has been exploited in photovoltaics and photocatalysis. The photocatalytic degradation of dyes and other environmental pollutants by heterogeneous ZnO nanomaterial catalysts is a thoroughly investigated area due to its immense potential in the low cost treatment of industrial effluents.<sup>1</sup> The degradation efficiency depends on the generation of electrons (conduction band) and holes (valence band) under UV light irradiation, which combine with oxygen and hydroxyl ions to form radicals that react with molecules. The recombination rate of electron–hole pairs seen as UV band edge emission affects the degradation rate and a faster recombination deters the degradation efficiency. Hence, there has been renewed interest in improving the efficiency of ZnO by

introducing defect levels or charge transfer states to suppress the recombination effects.<sup>2,3</sup> The defect engineering in the parent ZnO material in the form of oxygen and zinc vacancies or interstitials as trap states is shown to promote charge separation.<sup>3,4</sup> Combining ZnO nanostructures with noble metal nanoparticles and carbon nanostructures provides alternate charge transfer pathways prolonging the lifetime of electrons and holes.<sup>2,5</sup> Thus, Au–ZnO hybrid nanoarchitectures and Ag–ZnO heterostructures are found to be efficient photocatalysts than the ZnO constituent alone.<sup>6–11</sup> Photoluminescence studies and Kelvin probe microscopy uphold facile photoelectron transfer from ZnO to metal.<sup>6,12</sup> ZnO–carbon nanofibre heterostructures also exhibit higher photocatalytic rates with the evidence of charge transfer.<sup>13</sup> A further advantage of introducing defect states and metal nanoparticles is the extension of absorption characteristics in the visible region enabling the more economical visible light driven photocatalysis.<sup>7,14,15</sup> With the advent of 2D graphene, there have been several reports on the efficiency of ZnO hybrids with graphene or reduced graphene oxide (rGO) for the photocatalytic degradation of organic molecules.<sup>15,16</sup> This is facilitated by the excited state electron transfer from ZnO to graphene.<sup>17,18</sup> There are only a handful of reports on combining ZnO with rGO and metal nanoparticles for improved photodegradation.<sup>19,20</sup> ZnO–rGO–Au

<sup>a</sup> Centre for Nano and Soft Matter Sciences, Jalahalli, Bangalore-560013, India

<sup>b</sup> CSIR-National Physical Laboratory, Dr. K. S. Krishnan Road, New Delhi-110012, India. E-mail: jsneena@cens.res.in

† Electronic supplementary information (ESI) available: HRTEM of rGO–Au–ZnO, EDS results, photoluminescence and SEM of sintered rGO–ZnO nanorods and photodegradation rates for ZnO hybrid systems from literature. See DOI: 10.1039/c5cp05081b

heterostructures have also been utilized as bifunctional substrates for monitoring dye degradation *via* surface enhanced Raman scattering.<sup>21</sup>

Earlier reports have shown that different preparation methods greatly influence the morphology of ZnO nanostructures and also the defect states, which in turn affects emission characteristics and photocatalytic rates.<sup>4,22,23</sup> Pan *et al.* have employed GO as a surfactant to tune the morphology of ZnO nanostructures imparting oxygen defects in the ZnO lattice and explored the photocatalytic rates.<sup>15</sup> However, a thorough comparison of the degradation kinetics using rGO–ZnO hybrids having various ZnO morphologies or when they are combined with metal nanoparticles, in correlation to their structure and property, is lacking. Moreover, the role of rGO as a dye adsorbent in addition to its role as a charge transfer agent can remarkably affect the kinetics.<sup>24</sup> A comparison of the adsorption and charge transfer contributions of the hybrid catalyst towards higher photocatalytic rates could augment our understanding of the process. In this study, we have chosen the rGO–ZnO system grown under different synthesis conditions such as solution phase and hydrothermal routes to probe the effect of morphology and defect states of the ZnO nanostructures when combined with rGO layers or rGO–Au nanoparticles on the photodegradation rates of rhodamine B dye molecules. The photoluminescence exhibited by these composites gives insights into the possible defect states of the nanostructures and is related to the observed kinetics. The effect of dye adsorption by rGO on degradation kinetics is also addressed in this study.

## Experimental details

Bis(2,4-pentanedionate) zinc monohydrate (zinc acetylacetonate, Zn(acac)<sub>2</sub>·H<sub>2</sub>O), ammonia solution (25%), absolute ethanol (99.99%), hydrazine hydrate (NH<sub>2</sub>NH<sub>2</sub>·H<sub>2</sub>O), and rhodamine B (RB) were purchased from Sigma Aldrich and used as received. Exfoliated GO was synthesized from graphite powder (–300 mesh, Alfa-Aesar) employing modified Hummer's method.<sup>25</sup>

### Synthesis of rGO–ZnO and rGO–Au–ZnO hybrids

rGO and rGO–Au were prepared initially before loading ZnO *in situ*. rGO was prepared by the reduction of GO (3 mg in 25 mL of Milli-Q water) with hydrazine hydrate (20 μL). The mixture was heated at 90 °C for 2 h. The yellowish brown colour of GO changed to black coloured rGO dispersion, which was filtered, dried under vacuum and re-dispersed in ethanol. For the preparation of rGO–Au, 1 mL of 25 mM HAuCl<sub>4</sub> was also added to GO dispersion followed by reduction with hydrazine hydrate.

**Solution phase deposition.** rGO–ZnO was prepared by the addition of 300 μmoles of Zn(acac)<sub>2</sub> and 600 μmoles of ammonia to rGO dispersion (in 25 mL of ethanol) in a round-bottom flask followed by heating in an oil bath maintained at 120 °C for 8 h. The product was filtered, washed and dried. For the synthesis of rGO–Au–ZnO, rGO–Au dispersion was used instead of rGO in the above process. Bare ZnO without rGO support was also prepared in a similar manner, for comparison of properties.

**Hydrothermal route.** rGO–ZnO was prepared by adding 300 μmoles of Zn(acac)<sub>2</sub> and 600 μmoles of ammonia to rGO dispersion (in 20 mL of ethanol) in a Teflon lined stainless steel autoclave (pressure vessel) followed by heating in an oven at 120 °C for 8 h. After completion of the reaction, the autoclave was cooled down to room temperature. The product was collected and washed with Milli-Q water. The final product was dried at 50 °C.

### Characterization

UV-visible absorption spectra of the as-prepared rGO–ZnO hybrids were recorded on a Perkin-Elmer Lambda 20 spectrophotometer and the samples were dispersed in ethanol by sonication for this purpose. Photoluminescence (PL) of samples dispersed in ethanol was recorded using Horiba Jobin Yvon Fluorolog-3. X-ray diffraction (XRD) analysis of the samples was performed with a Rigaku Smart Lab diffractometer equipped with parallel beam optics and Cu-Kα radiation ( $\lambda = 1.54 \text{ \AA}$ , 40 kV, 30 mA) was incident at the grazing angle 0.3°. Field emission scanning electron microscopy (FESEM) and energy dispersive X-ray spectroscopy (EDS) were performed using a Nova Nano-SEM600 (FEL, The Netherlands). For SEM imaging, the dispersions were drop-cast on doped Si substrates and dried under argon gas. Backscattered secondary electron images were obtained using a dedicated solid-state backscattered secondary electron detector. EDS mapping of Au M, Zn L and C K levels was performed at 15 kV with a dwell time of 8 s per pixel.

### Photocatalytic studies

The photocatalytic activity of ZnO nanoparticles and ZnO hybrids was evaluated by monitoring the absorption of RB dye at 556 nm with time when irradiated with UV light (Hamamatsu L833-01 UV spot light source) of 365 nm wavelength and 110 mW cm<sup>–2</sup> power. UV-vis absorption spectra were acquired at regular intervals using a Perkin-Elmer Lambda 20 spectrophotometer. In a typical experiment, 10 mg of ZnO or its hybrids used as a catalyst was added to 50 mL of 40 μM RB solution (19 ppm) in a beaker. Before irradiation, the solution was stirred overnight in the dark to achieve adsorption equilibrium. Absorption spectra before and after stirring were also monitored. After overnight stirring, the solution was exposed to UV light. The distance between the lamp and the sample was kept at 4.5 cm, corresponding to 110 mW cm<sup>–2</sup> for 100% intensity. About 1 mL of sample was withdrawn at regular intervals during the experiment, diluted to 2 mL and centrifuged at 3000 rpm to extract the catalyst. The concentration of RB in the resultant solution was monitored by absorption spectra in the range of 400–700 nm. The absolute concentration was calculated from the measured absorbance values by applying Beer–Lambert law for standard RB solutions. For studying the effect of UV power on the photocatalysis of RB, rGO–ZnO prepared by hydrothermal route was used as the catalyst under similar reaction conditions described above except for varying light intensities, 100%, 73%, 51% and 27% corresponding to 110, 75, 50 and 25 mW cm<sup>–2</sup>, respectively. The light intensities of the UV lamp were measured using a photodiode positioned at a similar distance from the source as was the case for the samples.

## Results and discussion

ZnO is loaded on to rGO and rGO–Au hybrids by *in situ* reaction involving alkaline hydrolysis of zinc acetylacetonate in ethanol under two different synthesis conditions – solution phase and hydrothermal. ZnO and Au nanoparticles are prepared without any capping organic molecules. The as-synthesized products are characterized by XRD to assess the formation of ZnO, its structure and crystallinity. Fig. 1 gives the XRD patterns of ZnO, rGO–ZnO and rGO–Au–ZnO composites prepared under different synthesis conditions. ZnO prepared in solution phase (Fig. 1a) shows major reflections at  $31.8^\circ$  (100),  $34.4^\circ$  (002),  $36.3^\circ$  (101),  $47.6^\circ$  (102),  $56.7^\circ$  (110),  $62.9^\circ$  (103) and  $67.9^\circ$  (112) corresponding to hexagonal wurtzite structure. The rGO–ZnO nanohybrid (Fig. 1b) prepared in solution phase shows a pronounced amorphous peak at  $22^\circ$  from exfoliated rGO layers in addition to ZnO reflections. Fig. 1c shows the presence of gold along with ZnO and rGO in the case of rGO–Au–ZnO hybrid. Sharper diffraction peaks of higher intensity are observed for rGO–ZnO prepared under hydrothermal conditions when compared to the broad ones from solution phase ZnO. This indicates that highly crystalline and larger ZnO grains are formed under hydrothermal conditions involving higher temperature and pressure inside the autoclave.

UV-visible absorption spectra of ZnO and rGO–ZnO hybrids are given in Fig. 2. Solution phase prepared ZnO and rGO–ZnO hybrids exhibit band edge absorption at 355 nm, almost 15 nm blue-shifted than the band gap absorption of bulk ZnO at 370 nm (Fig. 2a and b). The blue shift arises from the quantum confinement effect of the smaller feature size of ZnO. In the case of rGO–ZnO (Fig. 2b), the band edge absorption extends slightly more into the visible region when compared to bare ZnO (Fig. 2a). Absorption at 280 nm is also observed in all the cases of rGO based hybrids arising from the  $\pi$ – $\pi^*$  transition of the  $sp^2$  hybridized carbon network in rGO (Fig. 2b–d). For rGO–Au–ZnO prepared in solution phase, the band edge absorption of ZnO is observed at 360 nm along with a broad absorption at  $\sim 600$  nm (Fig. 2c). Expanded view of the region between 350 and 1000 nm in the inset gives a clear view of the broad peak at 600 nm arising from the surface plasmon absorption of

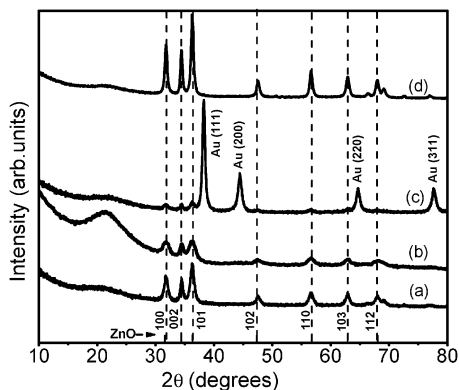


Fig. 1 XRD patterns of ZnO and rGO based ZnO hybrids obtained under different synthesis conditions. (a) ZnO, (b) rGO–ZnO, (c) rGO–Au–ZnO; by solution phase deposition, (d) rGO–ZnO by hydrothermal route.

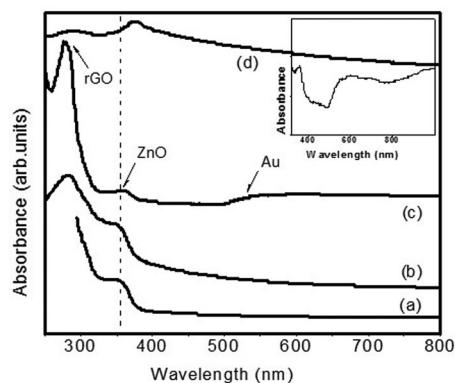
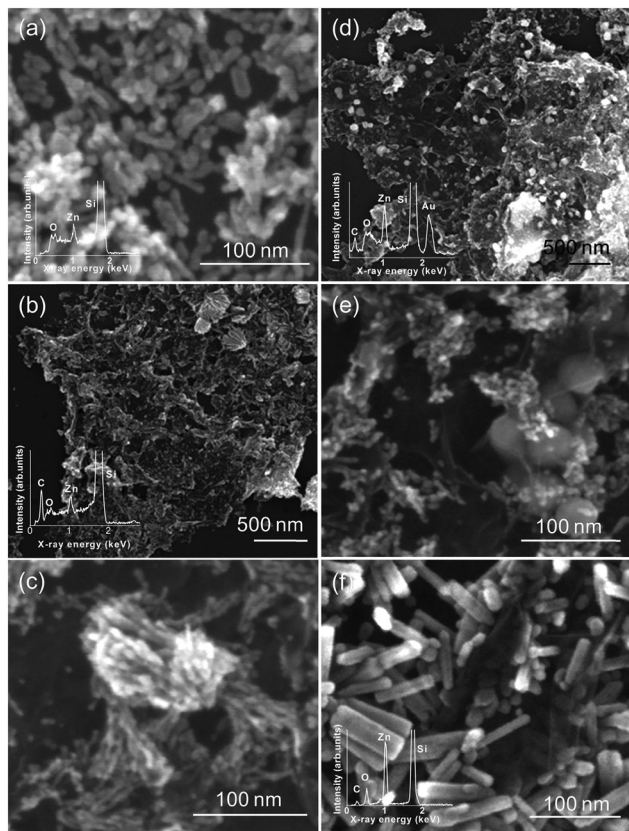


Fig. 2 UV-visible absorption spectra of ZnO and rGO based ZnO nanohybrids prepared under different synthesis conditions. (a) ZnO, (b) rGO–ZnO, (c) rGO–Au–ZnO; solution phase preparation. The inset shows the selected region of ZnO and Au nanoparticle absorption in (c). (d) rGO–ZnO by hydrothermal route.

Au nanoparticles on rGO. The band edge absorption of ZnO is observed at 373 nm, similar to that of bulk ZnO in the case of rGO–ZnO prepared by hydrothermal route. However, the absorption edge tails more into the visible region (Fig. 2d). The extension of band edge absorption of ZnO into the visible region often indicates the presence of defect levels contributed by Zn and O vacancies and interstitials encountered for different morphologies under various preparation conditions.<sup>3,4</sup>

The morphology, distribution and composition of ZnO and ZnO hybrids with rGO and Au nanoparticles (NPs) are studied by FESEM and EDS. Fig. 3a shows bare ZnO nanostructures obtained by solution phase deposition. ZnO nanostructures appear as spheroidal particles that aggregate to form slightly elongated structures. Similar aggregated ZnO spheroidal particles are obtained on rGO layers during the solution phase preparation of rGO–ZnO hybrids (Fig. 3b and c). In the magnified view given in Fig. 3c, bunches of aggregated, elongated nanostructures appear like grain stalks. When ZnO is grown *in situ* on to rGO–Au nanoparticle hybrids by solution phase growth, aggregated particles are observed (Fig. 3d and e). Au nanoparticles appear as bright spheres of 30–100 nm diameter interspersed with rGO layers and ZnO particles are seen interfaced with Au nanoparticles or rGO layers (Fig. 3e). The size distribution of Au NPs obtained from SEM images is given in Fig. S1 (ESI<sup>†</sup>). EDS spectra given in the inset of Fig. 3d show the presence of Au along with Zn, O and carbon. rGO–ZnO hybrids prepared under hydrothermal conditions exhibit well-defined hexagonal ZnO rods with  $\sim 20$  nm diameter and 60–80 nm length on rGO flakes (Fig. 3f). Higher temperature and pressure achieved inside the hydrothermal vessel produce highly crystalline, well-shaped ZnO nanorods (NRs) compared to solution phase prepared samples. We have observed that the yield of rGO–ZnO obtained under hydrothermal conditions is almost 3 times higher than that obtained by solution phase preparation for similar quantities of precursors and duration of reaction indicating an efficient hydrolysis of the zinc oxide precursor and completion of reaction under hydrothermal conditions. A gravimetric assay in the lab by oxidising rGO in air gave the weight percentage for ZnO:rGO



**Fig. 3** FESEM and EDS of ZnO and its hybrids prepared under different synthesis conditions. (a) ZnO by solution phase, (b) rGO-ZnO by solution phase; ZnO nanostructures interspersed with rGO layers. (c) A magnified view of (b); aggregated elongated ZnO features bunched like grain stalks. (d) rGO-Au-ZnO by solution phase; Au nanoparticles and ZnO features on rGO layers. (e) A magnified view of (d); bright spheres are Au nanoparticles and ZnO particles appear as aggregated nanoparticles. (f) rGO-ZnO by hydrothermal route; well-defined hexagonal rods of ZnO mixed with rGO flakes. EDS spectra given in the insets of (a), (b), (d) and (f) show the elemental composition of the respective materials (Si signal is from the substrate).

roughly as 72:28 for hydrothermally prepared rGO-ZnO NRs and 48:52 for solution phase prepared rGO-ZnO NPs. The weight percentage of ZnO:rGO:Au is 50:30:20 for rGO-Au-ZnO NP hybrids as calculated from gravimetric and EDS analysis. The elemental compositions obtained from EDS for various products are given in the ESI† (Table S1). The carbon to zinc atomic ratio is lower in the case of hydrothermal product than solution phase product in accordance with the gravimetric assay. The Zn to oxygen atomic ratio is observed to be lower in the solution phase prepared bare ZnO NPs indicating a higher concentration of Zn vacancies and defects in the solution phase prepared hybrids.

In order to show the distribution and interfacial of Au nanoparticles with ZnO and rGO in the ternary GO-Au-ZnO hybrids, we further performed back scattered secondary electron imaging and EDS mapping of the constituents. Fig. 4 shows the secondary electron image and the corresponding backscattered secondary electron image of a region of the rGO-Au-ZnO hybrid. The nanoparticles of Au having the highest backscattering

coefficient appear as the brightest spheres in the backscattered image and ZnO nanostructures on rGO appear less bright (Fig. 4b). Isolated ZnO nanostructures are not easily discernible in the backscattered image as they possess a low scattering coefficient. EDS mapping of a selected region of the above hybrid is performed for Au M, Zn L and C K levels. An Au M map and a composite map of C, Zn, Au along with the corresponding secondary electron image are given in Fig. 4c–e. The mapped elements are represented by different colours.

High resolution TEM (Fig. 5) has been performed to have a closer look at rGO-ZnO interfaces and Au-ZnO interfaces with rGO in hybrid materials. Fig. 5a shows the shape of ZnO NPs prepared by solution route in the absence of rGO. The particles are slightly elongated and a few are aggregated to form elongated structures which are also observed in FESEM images (Fig. 3a). HRTEM images of individual ZnO particles (Fig. 5b) show  $d$  spacings of 2.8 Å and 2.6 Å corresponding to (100) and (002) lattice planes of wurtzite ZnO, respectively. FFT of an ensemble of lattice resolved ZnO NPs (inset of Fig. 5b) gives reflections corresponding to  $d_{100}$ ,  $d_{002}$  and  $d_{101}$ . Fig. 5c shows some isolated ZnO NPs on rGO for the rGO-ZnO hybrid obtained by solution deposition and Fig. 5d gives the lattice resolution of ZnO NPs corresponding to (100) (2.8 Å) and (112) (2.7 Å) planes. Fig. 5e shows the TEM image of the rGO-Au-ZnO NP hybrid material. The nanoparticles are seen embedded in the rGO film. The high resolution image (Fig. S2, ESI† and Fig. 5f) differentiates Au NPs and ZnO NPs clearly. Au NPs appear darker compared to ZnO in the bright field TEM images due to their high scattering coefficient. Smaller Au NPs of 10–15 nm size are more clearly observed in high resolution TEM images and hence are focused for analysis. Fig. 5f shows HRTEM of a single Au NP along with ZnO nanoparticles embedded in rGO layers. The lattice fringes corresponding to (111) and (200) planes with multiple domains are seen belonging to polycrystalline fcc structure of gold. FFT of the marked region of Au NP also confirms the observation. The lattice fringes of ZnO NPs indicated in Fig. 5f correspond to (110) and (101) planes of wurtzite ZnO. (002) and (100) lattice planes of

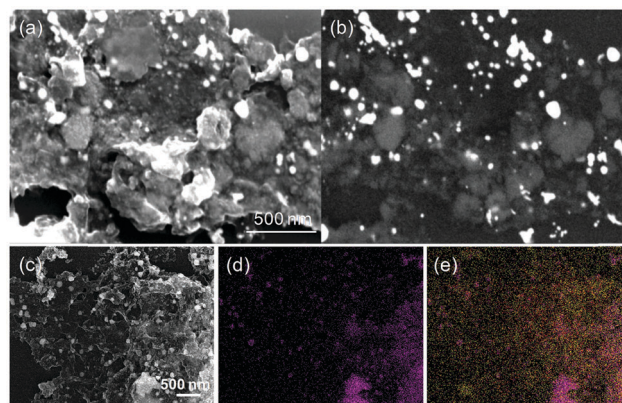


**Fig. 4** FESEM images of the rGO-Au-ZnO nanohybrid. (a) Secondary electron image and the corresponding backscattered image (b). (c) Secondary electron image and the corresponding EDS map of Au M level (d) and the combined EDS map (e) of C K (red), Au M (magenta) and Zn L (yellow).

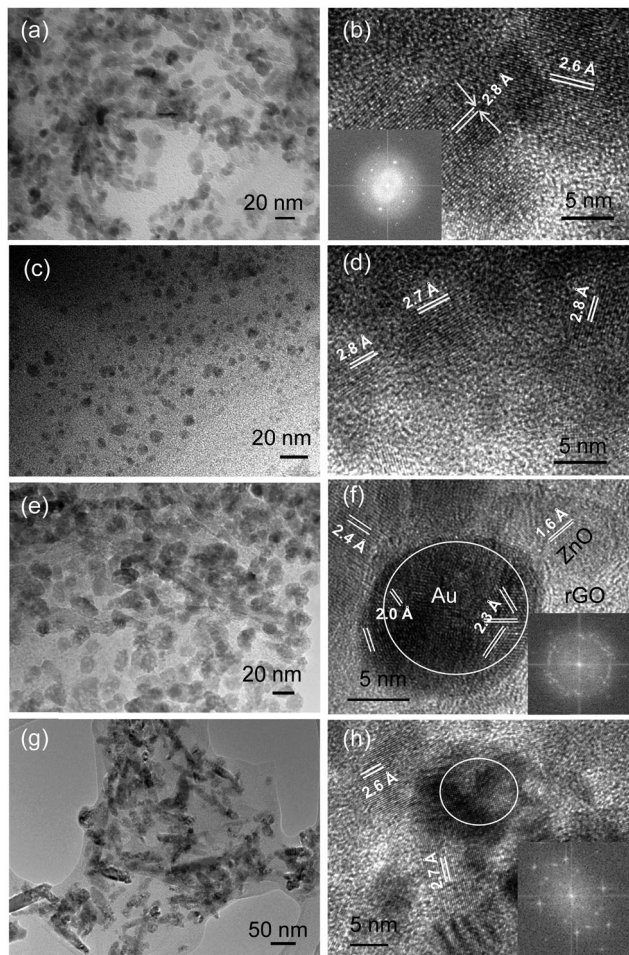


**Fig. 5** TEM images of various rGO based ZnO hybrids. (a) ZnO NPs obtained by solution route. (b) High resolution image of ZnO particles given in (a) showing lattice fringes of ZnO. The inset gives the FFT of the HRTEM image. (c) rGO-ZnO NPs obtained by solution route. (d) High resolution images of ZnO NPs on rGO. (e) rGO-Au-ZnO NPs prepared by solution route. (f) High resolution images of (e) showing the lattice of Au NPs and ZnO NPs on rGO. Au-ZnO interfaces with rGO can be seen. The inset gives FFT of the marked Au NP region. (g) rGO-ZnO NRs obtained by hydrothermal route. (h) High resolution image of ZnO nanorods on rGO. The inset gives FFT of the marked region.

ZnO are also observed in the same sample (Fig. S2, ESI<sup>†</sup>). Interestingly, the Au-ZnO-rGO interface is clearly observed, as marked in HRTEM images (Fig. 5f and Fig. S2, ESI<sup>†</sup>). Fig. 5g shows TEM of rGO-ZnO NRs prepared by hydrothermal reaction. ZnO nanorods (NRs) are seen embedded in the rGO film. High resolution images (Fig. 5h) show lattice fringes with  $d_{002}$  (2.6 Å) and  $d_{112}$  (2.7 Å) spacings of wurtzite ZnO. (002) planes are majorly seen along (100) (*c*-axis) for nanorods. FFT (inset of Fig. 5h) of a region where a few rods overlap (marked by a circle in Fig. 5h) gives reflections corresponding to (110), (100), (112), (002) and (101) lattice planes of ZnO. Additional HRTEM images of rGO-ZnO rods are shown in Fig. S3 (ESI<sup>†</sup>).

Optical properties of ZnO nanocrystallites provide an understanding of the defect states and donor-acceptor levels and are usually probed by photoluminescence.<sup>26</sup> The PL spectra given

in Fig. 6 exhibit spontaneous excitonic emission (band-edge) from ZnO nanostructures at 380 nm (indicated by an arrow in Fig. 6) along with various defect emissions in the visible region for ZnO and rGO-ZnO hybrids prepared by different synthetic routes. rGO itself (Fig. 6a) exhibits a low intensity PL in the violet-blue region (around ~420 nm), which may arise from the radiative recombination of e-h pairs due to small  $sp^2$  clusters embedded in the  $sp^3$  matrix.<sup>27</sup> Bare ZnO nanoparticles prepared in solution phase exhibit intense defect emissions in the visible region at ~405, 430 and 460 nm (Fig. 6b), which are often associated with intrinsic ZnO defects such as zinc vacancies ( $V_{Zn}$ )/zinc interstitials ( $Zn_i$ ).<sup>28,29</sup> In the case of rGO-ZnO NPs prepared by solution route, the defect emissions are seen extending into the yellow-green region (Fig. 6c). The green emissions arise mainly from oxygen vacancies on surfaces and have been reported in the case of ZnO obtained by the hydrolysis of the zinc acetylacetonate precursor.<sup>30</sup> However, the band edge as well as defect emissions are seen largely quenched due to the presence of rGO.<sup>18,31</sup> For the rGO-Au-ZnO NP system prepared by solution phase, the band edge emission is seen largely quenched while visible defect emissions seen in the violet-blue-green regions are only slightly quenched. rGO-ZnO NRs prepared under hydrothermal conditions show luminescence in the green-yellow region, indicating the presence of surface defects and oxygen interstitials.<sup>3,29</sup> Band edge emission is reduced compared to bare ZnO but intense than that observed for rGO-ZnO NPs obtained by solution route.

The potential application of rGO based ZnO composites in photocatalysis is studied in detail by monitoring the degradation of RB, a fluorescent dye, by UV-vis spectroscopy. A 40  $\mu$ M solution of RB is irradiated with UV spot light of intensity 110  $mW\ cm^{-2}$  in the absence and presence of catalysts (10 mg) until the solution appeared colourless. Fixed aliquots of solution are withdrawn at specific time intervals and the absorbance at 556 nm is monitored. The decrease of RB absorbance with irradiation time for the catalyst rGO-Au-ZnO is shown in Fig. 7a. Within 45 min, RB degradation is almost complete. From the absorbance values, the residual concentrations of RB is calculated by applying

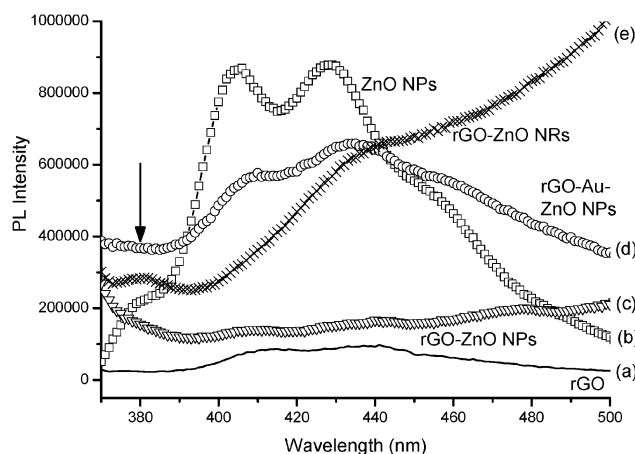


**Fig. 6** PL spectra of ZnO hybrids ( $\lambda_{ex}$  – 325 nm). (a) rGO, (b) bare ZnO NPs (intensity/2 is given), (c) rGO-ZnO NPs, (d) rGO-Au-ZnO NPs, by the solution phase method, and (e) rGO-ZnO NRs by the hydrothermal method.

Beer–Lamberts law, and the kinetics of the photodegradation of RB in the presence of various catalysts such as bare ZnO NPs, rGO–ZnO NPs, and rGO–Au–ZnO NPs prepared by conventional solution methods and rGO–ZnO NRs prepared by the hydrothermal method are evaluated.  $C_t/C_0$  vs. irradiation time is plotted and given in Fig. 7b, where  $C_t$  is RB concentration at a given time during irradiation and  $C_0$  is the RB concentration after overnight equilibration with the catalyst before irradiation and is taken as concentration at zero time.

It is clearly seen that the photodegradation rates of the various catalysts follow the order rGO–Au–ZnO NPs > rGO–ZnO NPs > rGO–ZnO NRs > bare ZnO NPs. Most of the previous studies have shown that the dye degradation kinetics follow a pseudo first order kinetics derived from the Langmuir–Hinshelwood mechanism for low reactant concentrations (eqn (1)).

$$C_t = C_0 e^{-k_{\text{obs}} t} \quad (1)$$

In the present study, we also see that for lower irradiation times, the plots in Fig. 7b can be fitted with eqn (1) and the values of  $k_{\text{obs}}$  obtained for various photocatalysts are  $0.065 \text{ min}^{-1}$  (rGO–Au–ZnO NPs),  $0.046 \text{ min}^{-1}$  (rGO–ZnO NPs),  $0.033 \text{ min}^{-1}$  (rGO–ZnO NRs) and  $0.0135 \text{ min}^{-1}$  (bare ZnO NPs). Hence, rGO–Au–ZnO NPs provide a degradation rate almost 5 times faster than bare ZnO NPs and 1.5 times faster than rGO–ZnO NPs. The degradation efficiency, calculated as  $\frac{C_0 - C_t}{C_0} \times 100$ , for the above hybrid photocatalysts is compared in Fig. 7c. At 40 min, 96% of RB has

undergone degradation in the presence of rGO–Au–ZnO NP catalyst while it is 84% for rGO–ZnO NPs and only 67% for rGO–ZnO NRs (hydrothermal route). Bare ZnO NPs could achieve only 36% degradation in comparison to the hybrid ones. It is observed that during the initial 20 min irradiation, the degradation % in the presence of rGO–ZnO NRs is slightly greater than for rGO–ZnO NPs. To compare with a recently reported result of methylene orange degradation by rGO–ZnO–Ag NPs, the reported degradation efficiency is only 94% in 68 min.<sup>19</sup> In another case of RB degradation using rGO–ZnO NPs, complete degradation is achieved in 60 min.<sup>32,33</sup> However, a one to one comparison with literature values is difficult since the degradation rates are largely dependent on the irradiation power, amount of catalyst and dye concentration. We have provided a comparative table of the reported rate values for various systems in Table S2 (ESI†).

The kinetics of RB photodegradation is also studied by varying the power/intensity of the incident UV light for the catalyst, rGO–ZnO NRs, keeping all other experimental parameters constant. In Fig. 7d, the normalized residual concentrations of RB with time when irradiated with a UV light of 50, 75 and  $110 \text{ mW cm}^{-2}$  are shown. As expected, the degradation rate increases with the increase in incident power. The observed rate constants ( $k_{\text{obs}}$ ) vary with light intensity ( $I$ ) as  $k_{\text{obs}} = I^{0.74}$  (Fig. 7d inset). In the previous photodegradation studies reported in the literature, the rate varies as the square root of intensity at higher light intensities and in some cases it is between 0.5 and 1. Linear variation has been observed only at sufficiently low intensities.<sup>34</sup>

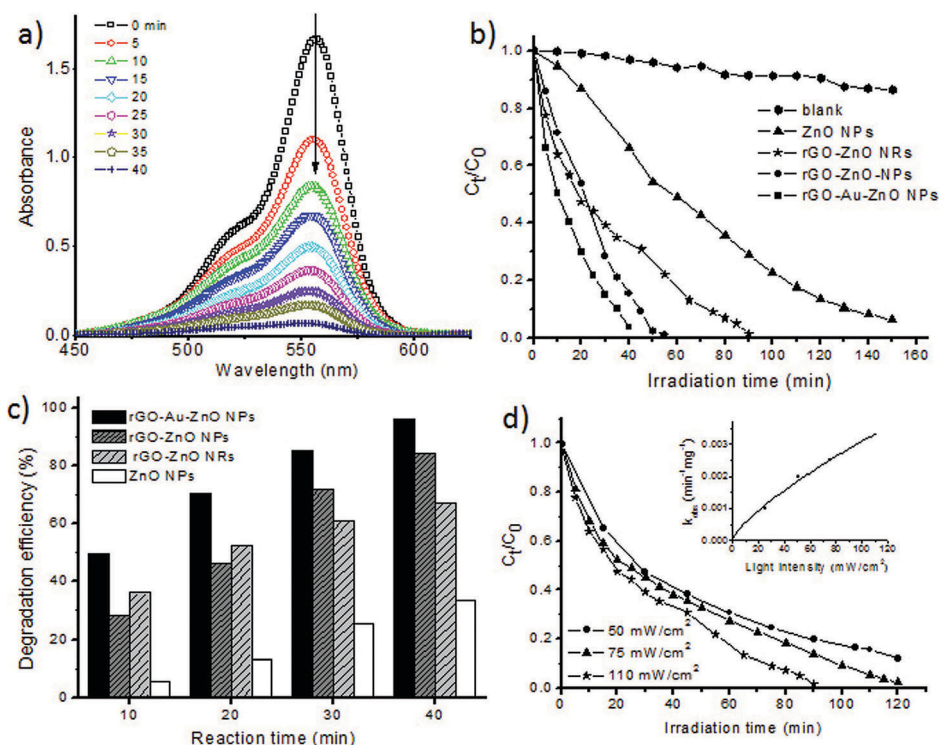


Fig. 7 (a) Time evolution of the UV-vis spectra of  $40 \mu\text{M}$  RB dye solution in the presence of rGO–Au–ZnO NP catalyst when irradiated with  $365 \text{ nm}$  light of intensity  $110 \text{ mW cm}^{-2}$ . (b) Kinetics of  $40 \mu\text{M}$  RB dye degradation in the absence and presence of various catalysts (10 mg), bare ZnO NPs, rGO–ZnO NPs, rGO–ZnO NRs and rGO–Au–ZnO NPs. (c) Degradation efficiency of various catalysts for RB dye till 40 min of irradiation time. (d) Kinetics of RB degradation at various light intensities for the rGO–ZnO NR catalyst; the inset shows the variation of the observed rate constant with light intensity.

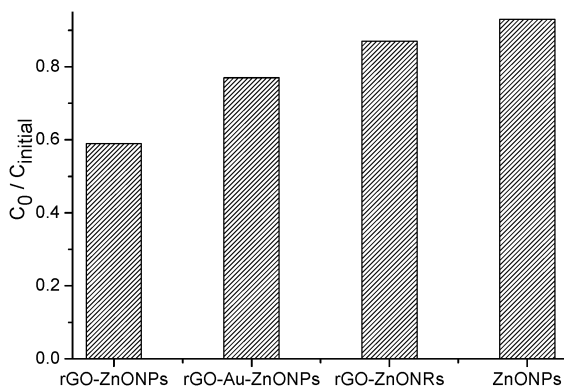


Fig. 8 The ratio of equilibrium concentration to initial concentration for various photocatalysts.

Apart from the fact that rGO acts as a medium for charge transport reducing the recombination rates, it also acts as a good adsorbent for pollutants like activated carbon.<sup>20,24</sup> During the photodegradation studies of RB using rGO-ZnO hybrids, we have observed that RB molecules get adsorbed on rGO based hybrids more than that on bare ZnO. The adsorption is evident from the reduced absorbance of RB solution observed in the UV-vis spectra, obtained after overnight equilibration with the catalyst in the dark (considered as  $C_0$ ). Hence, for rGO-ZnO NRs, the initial concentration of 40  $\mu\text{M}$  RB has reduced to 35  $\mu\text{M}$  after equilibration. This decrease in concentration is found to increase with the increase in the rGO content of the catalyst. The bar chart in Fig. 8 shows the ratio of equilibrium concentration (in the presence of catalyst) to initial concentration of RB (before adding catalyst) for various catalysts in the order of increasing rGO content. The adsorption capacity of the hybrids can be calculated as  $Q = \frac{(C_{\text{initial}} - C_0)V}{m}$ , where  $Q$  is the adsorption at equilibrium ( $\text{mg g}^{-1}$ ),  $V$  is the volume of the solution and  $m$  is the mass of the catalyst.  $C_{\text{initial}}$  and  $C_0$  are defined as above and expressed in  $\text{mg L}^{-1}$ . The adsorption capacity of rGO-ZnO NPs is 37.7  $\text{mg g}^{-1}$  while that of rGO-Au-ZnO NPs, rGO-ZnO NRs and bare ZnO NPs is 23.8, 11.9 and 6.4  $\text{mg g}^{-1}$  respectively. An adsorption capacity of 32.6  $\text{mg g}^{-1}$  has been reported for rGO-ZnO previously. It is noticeable that though rGO-ZnO NPs have the highest adsorption capacity, they have a lower degradation rate than rGO-Au-ZnO NPs, which is discussed below.

### Discussion: structure–property correlation

The photocatalytic rates clearly improved in the presence of rGO or rGO-Au nanoparticles along with ZnO (Fig. 7), in accordance with the previous studies.<sup>15,16,19–21,35–37</sup> Enhancement in photocatalytic rates arises due to charge transfer between ZnO and other components of the hybrid, thereby suppressing the recombination of electrons and holes in photoexcited ZnO. The charge separation leads to increased lifetimes of holes and electrons, which are now available for reaction with hydroxyl ions and oxygen generating hydroxyl and superoxide radicals that are responsible for the oxidation and further degradation of RB dye.<sup>13</sup>

Various possible charge transfer mechanisms upon irradiation are (1) excited state electron transfer from the conduction band and defect levels of ZnO to rGO and Au, (2) excited state electron transfer from the RB molecule to ZnO, rGO and Au energy levels and (3) surface plasmon enhanced electron transfer from Au to ZnO. The last two mechanisms are more probable for visible light irradiation.<sup>38</sup> In this study employing UV irradiation, the first mechanism is more plausible. *In situ* synthesis of the hybrids generates intimate physical interfaces between the components (Fig. 5) facilitating band bending and charge transfer. The nature of charge transfer is reflected in the PL spectra of rGO-ZnO hybrids as suppression in the UV band edge emission peaks at 380 nm and visible defect emission peaks (Fig. 6). Here, rGO acts as an acceptor and 2D conductor for shuttling of photoexcited electrons from the ZnO conduction band and defect levels.<sup>18,31</sup> We have removed rGO selectively from rGO-ZnO NRs by sintering and subjected them to PL and photocatalysis. The PL spectra indeed show a revival of band edge and visible emissions of ZnO (Fig. S4, ESI†). The morphology of ZnO NRs after sintering is seen unaltered. The photodegradation rate is also observed to be very slow, one order less than the hybrid.

rGO-Au-ZnO NPs provide the highest photocatalytic rate (Fig. 7) since both rGO and Au components can participate in the charge separation thereby limiting exciton recombinations. This is reflected in the PL spectra (Fig. 6) as a highly quenched band edge emission peak. This indicates that Au levels offer an alternate pathway for the transfer of photoexcited electrons from the ZnO conduction band. Charge transfer studies of Au-ZnO nanoparticle systems have shown that the Au nanocore can store electrons until the equilibration of Fermi level with the ZnO conduction band and are readily available for discharge.<sup>5,37,39</sup> However, the defect emissions in the visible violet-blue region are not greatly affected as compared to rGO-ZnO NPs. This indicates that the electron or hole transfer from defect states of  $V_{\text{Zn}}/Zn_i$  to Au or rGO is probably not favoured as in the case of oxygen vacancy states of ZnO to rGO, and additionally, rGO content is comparatively low in this case. This has also been observed for rGO-ZnO-Ag composites.<sup>19</sup> With the inclusion of Au NPs in rGO-ZnO, the surface plasmon scattering might also cause enhanced emission in the visible region which has been utilized by other researchers for visible light driven photocatalysis.<sup>14</sup>

rGO-ZnO NRs prepared by hydrothermal route exhibit a lower photocatalytic rate compared to rGO-ZnO NPs prepared by solution route. This indicates a lesser suppression in the charge carrier recombination which is indeed seen as a conspicuous band edge emission in the PL spectra (Fig. 6). This is due to lower rGO to ZnO ratio for hydrothermally prepared rGO-ZnO NRs compared to solution route hybrids. Additionally, the nanorod morphology can also contribute to lower photodegradation rates. It has been observed earlier that the surface of ZnO nanorods has mostly nonpolar facets while spheroidal nanoparticles may have more polar facets that facilitate hydroxyl ion adsorption.<sup>23</sup> From Fig. 7c, we notice that during the initial 20 min of irradiation, rGO-ZnO NRs provide a slightly higher dye degradation rate than rGO-ZnO

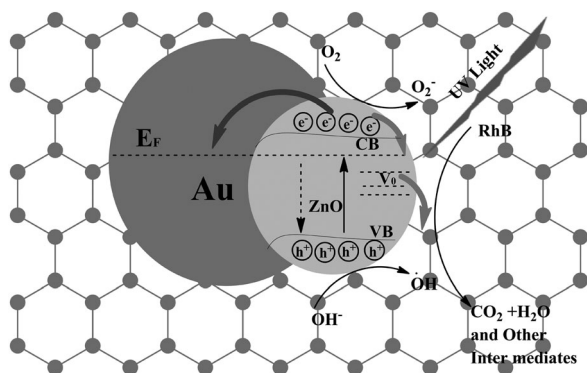


Fig. 9 A schematic diagram of the possible charge transfer processes in rGO–Au–ZnO NP hybrids during photodegradation of the dye.

NPs, which can be attributed to higher UV absorption as a consequence of higher ZnO content. After the initial surge, the charge separation provided by rGO controls the degradation rate. A schematic diagram of the charge transfer process is shown in Fig. 9.

rGO being a good adsorbent of the dyes, as seen from Fig. 8, can also affect the photocatalytic rate as the rate is proportional to the available adsorption sites or surface coverage according to the Langmuir–Hinshelwood mechanism.<sup>40</sup> Hence, according to Fig. 8, rGO–ZnO NPs having the highest rGO content and accordingly higher adsorption capacity should provide the highest degradation rate, followed by rGO–Au–ZnO NPs and rGO–ZnO NRs. However, the observed rate is highest for rGO–Au–ZnO NPs and the rates of rGO–ZnO NPs and rGO–ZnO NRs are close indicating that the photodegradation rates are more influenced by the suppression of electron–hole recombination due to charge transfer facilitated by Au and rGO constituents in the ternary hybrid system than a higher surface coverage.

## Conclusions

We have shown that various preparation routes can be used to obtain binary rGO–ZnO hybrid systems with ZnO bearing different morphologies. Solution phase and hydrothermal methods produced nanoparticle and nanorod morphologies of ZnO, respectively, on rGO. Ternary hybrid rGO–Au–ZnO has also been obtained by the solution phase method. Structural studies by high resolution electron microscopy reveal excellent interfacial contact between the constituents of the hybrid. The synthetic route influences the crystallinity of ZnO nanostructures, defect type and also rGO content in the hybrids, which in turn affect the photodegradation rates. Band edge and visible luminescence is quenched in hybrids due to the suppression of electron–hole recombinations, and accordingly, higher photodegradation rates are provided by hybrids than bare ZnO nanocrystals. Among the hybrids, rGO–Au–ZnO exhibits the highest rate,  $0.065 \text{ min}^{-1}$ , which is five times that of bare ZnO prepared by the same route. rGO–ZnO nanoparticles and rGO–ZnO nanorods exhibit rates of  $0.046$  and  $0.033 \text{ min}^{-1}$ , respectively. rGO and Au components serve as mediums for easy discharge of excited state electrons from ZnO

and the efficiency is reduced when only one component is present. Larger rGO content and morphology are deemed responsible for higher activity of solution phase prepared nanoparticle hybrids than hydrothermally prepared nanorod hybrids. Though the dye adsorption capability of rGO in the hybrids favors the degradation kinetics, the charge separation provided by the hybrid components is more influential. The effect of light intensity on degradation rates is studied and expressed as a power law variation.

## Acknowledgements

The authors would like to thank DST Unit on Nanoscience, JNCASR, for electron microscope facility. N. R. Selvi is acknowledged for technical assistance.

## References

- M. R. Hoffmann, S. T. Martin, W. Choi and D. W. Bahnemann, *Chem. Rev.*, 1995, **95**, 69–96.
- Q. Wang, B. Geng and S. Wang, *Environ. Sci. Technol.*, 2009, **43**, 8968–8973.
- Y. Zheng, C. Chen, Y. Zhan, X. Lin, Q. Zheng, K. Wei, J. Zhu and Y. Zhu, *Inorg. Chem.*, 2007, **46**, 6675–6682.
- L. Xu, Y. Hu, C. Pelligra, C. Chen, L. Jin, H. Huang, S. Sithambaram, M. Aindow, R. Joesten and S. L. Suib, *Chem. Mater.*, 2009, **21**, 2875–2885.
- V. Subramanian, E. E. Wolf and P. V. Kamat, *J. Phys. Chem. B*, 2003, **107**, 7479–7485.
- D. Lin, H. Wu, R. Zhang and W. Pan, *Chem. Mater.*, 2009, **21**, 3479–3484.
- P. Fageria, S. Gangopadhyay and S. Pande, *RSC Adv.*, 2014, **4**, 24962–24972.
- Y. Zheng, L. Zheng, Y. Zhan, X. Lin, Q. Zheng and K. Wei, *Inorg. Chem.*, 2007, **46**, 6980–6986.
- P. Li, Z. Wei, T. Wu, Q. Peng and Y. Li, *J. Am. Chem. Soc.*, 2011, **133**, 5660–5663.
- F. Xiao, F. Wang, X. Fu and Y. Zheng, *J. Mater. Chem.*, 2012, **22**, 2868–2877.
- R. Georgekutty, M. K. Seery and S. C. Pillai, *J. Phys. Chem. C*, 2008, **112**, 13563–13570.
- Y. Sung, V. D. Frolov, S. M. Pimenov and J. Wu, *Phys. Chem. Chem. Phys.*, 2012, **14**, 14492–14494.
- J. Mu, C. Shao, Z. Guo, Z. Zhang, M. Zhang, P. Zhang, B. Chen and Y. Liu, *ACS Appl. Mater. Interfaces*, 2011, **3**, 590–596.
- C. Mondal, J. Pal, M. Ganguly, A. K. Sinha, J. Jana and T. Pal, *New J. Chem.*, 2014, **38**, 2999–3005.
- X. Pan, M. Yang and Y. Xu, *Phys. Chem. Chem. Phys.*, 2014, **16**, 5589–5599.
- L. Zhang, L. Du, X. Cai, X. Yu, D. Zhang, L. Liang, P. Yang, X. Xing, W. Mai, S. Tan, Y. Gu and J. Song, *Physica E*, 2013, **47**, 279–284.
- P. Xu, Q. Tang and Z. Zhou, *Nanotechnology*, 2013, **24**, 305401.
- G. Williams and P. V. Kamat, *Langmuir*, 2009, **25**, 13869–13873.
- S. Sarkar and D. Basak, *CrystEngComm*, 2013, **15**, 7606–7614.

- 20 P. Roy, A. P. Periasamy, C. Liang and H. Chang, *Environ. Sci. Technol.*, 2013, **47**, 6688–6695.
- 21 C. Wen, F. Liao, S. Liu, Y. Zhao, Z. Kang, X. Zhang and M. Shao, *Chem. Commun.*, 2013, **49**, 3049–3051.
- 22 L. Wang, L. Chang, B. Zhao, Z. Yuan, G. Shao and W. Zheng, *Inorg. Chem.*, 2008, **47**, 1443–1452.
- 23 A. McLaren, T. Valdes-Solis, G. Li and S. C. Tsang, *J. Am. Chem. Soc.*, 2009, **131**, 12540–12541.
- 24 J. Wang, T. Tsuzuki, B. Tang, X. Hou, L. Sun and X. Wang, *ACS Appl. Mater. Interfaces*, 2012, **4**, 3084–3090.
- 25 W. S. Hummers and R. E. Offeman, *J. Am. Chem. Soc.*, 1958, **80**, 1339.
- 26 A. B. Djurišić and Y. H. Leung, *Small*, 2006, **2**, 944–961.
- 27 G. Eda, Y. Lin, C. Mattevi, H. Yamaguchi, H. Chen, I. Chen, C. Chen and M. Chhowalla, *Adv. Mater.*, 2010, **22**, 505–509.
- 28 H. Zeng, G. Duan, Y. Li, S. Yang, X. Xu and W. Cai, *Adv. Funct. Mater.*, 2010, **20**, 561–572.
- 29 D. Li, Y. H. Leung, A. B. Djurišić, Z. T. Liu, M. H. Xie, S. L. Shi, S. J. Xu and W. K. Chan, *Appl. Phys. Lett.*, 2004, **85**, 1601–1603.
- 30 E. Rauwel, A. Galeckas, P. Rauwel, M. F. Sunding and H. Fjellvag, *J. Phys. Chem. C*, 2011, **115**, 25227–25233;
- H.-M. Xiong, D.-P. Liu, Y.-Y. Xia and J.-S. Chen, *Chem. Mater.*, 2005, **17**, 3062–3064; X. Liu and M. T. Swihart, *Nanoscale*, 2013, **5**, 8029–8036.
- 31 Y. H. Ng, I. V. Lightcap, K. Goodwin, M. Matsumura and P. V. Kamat, *J. Phys. Chem. Lett.*, 2010, **1**, 2222–2227.
- 32 B. Li and H. Cao, *J. Mater. Chem.*, 2011, **21**, 3346–3349.
- 33 Q. Zhang, C. Tian, A. Wu, T. Tan, L. Sun, L. Wang and H. Fu, *J. Mater. Chem.*, 2012, **22**, 11778–11784.
- 34 D. Chen and A. K. Ray, *Water Res.*, 1998, **32**, 3223–3234.
- 35 X. Bai, L. Wang, R. Zong, Y. Lv, Y. Sun and Y. Zhu, *Langmuir*, 2013, **29**, 3097–3105.
- 36 N. P. Herring, S. H. Almahoudi, C. R. Olson and M. S. El-Shall, *J. Nanopart. Res.*, 2012, **14**, 1277.
- 37 Y. Yokomizo, S. Krishnamurthy and P. V. Kamat, *Catal. Today*, 2013, **199**, 36–41.
- 38 M. Yue, M. Yang, D. Zhang, D. Xiang, Y. Hou and J. Han, *J. Phys. Chem. C*, 2015, **119**, 4199–4207.
- 39 A. Wood, M. Giersig and P. Mulvaney, *J. Phys. Chem. B*, 2001, **105**, 8810–8815.
- 40 H. Al-Ekabi and N. Serpone, *J. Phys. Chem.*, 1988, **92**, 5726–5731.